Letter | Editors' Suggestion

Antiferromagnetic fluctuations and orbital-selective Mott transition in the van der Waals ferromagnet $Fe_{3-x}GeTe_2$

Xiaojian Bai,[1,*] Frank Lechermann,[2,†] Yaohua Liu,[1] Yongqiang Cheng,[1] Alexander I. Kolesnikov,[1] Feng Ye,[1] Travis J. Williams,[1] Songxue Chi,[1] Tao Hong,[1] Garrett E. Granroth,[1] Andrew F. May,[3] and Stuart Calder[1,‡]

[1]*Neutron Scattering Division, Oak Ridge National Laboratory, Oak Ridge, TN 37831, USA*

[2]*Institut für Theoretische Physik III, Ruhr-Universität Bochum, D-44780 Bochum, Germany*

[3]*Materials Science & Technology Division, Oak Ridge National Laboratory, Oak Ridge, TN 37831, USA*

(Received 3 February 2022; revised 26 August 2022; accepted 8 November 2022; published 30 November 2022)

$Fe_{3-x}GeTe_2$ is a layered magnetic van der Waals material of interest for both fundamental and applied research. Despite the observation of intriguing physical properties, open questions exist even on the basic features related to magnetism: is it a simple ferromagnet or are there antiferromagnetic regimes, and are the moments local or itinerant. Here, we demonstrate that antiferromagnetic spin fluctuations coexist with the ferromagnetism through comprehensive elastic and inelastic neutron scattering and thermodynamic measurements. Our realistic dynamical mean-field theory calculations reveal that the competing magnetic fluctuations are driven by an orbital selective Mott transition (OSMT), where only the plane-perpendicular a_{1g} orbital of the Fe($3d$) manifold remains itinerant. Our results highlight the multi-orbital character in $Fe_{3-x}GeTe_2$ that supports a rare coexistence of local and itinerant physics within this material.

DOI: 10.1103/PhysRevB.106.L180409

Reducing the dimensionality of a compound to topologically constrained layers can enhance quantum phenomena and drive novel behavior. In this context two-dimensional (2D) layered materials that can exist from the bulk down to single layers due to weak interlayer van der Waals (vdW) bonding have undergone intense interest [1,2]. The iron chalcogenide $Fe_{3-x}GeTe_2$ (FGT) [see Fig. 1(a)] has emerged as one of the central protagonists in 2D vdW material research. FGT is a rare example of a ferromagnetic (FM) metal vdW material, with the magnetism remaining robust down to the monolayer [3–6], making it promising for device applications [7,8]. Ionic gating has enhanced the magnetic ordering to room temperature in exfoliated flakes [3,9]. Additionally, there have been observations of anomalous Hall effect [10–12], large anomolous Nernst effect with Berry curvature [8], and bubble and labyrinth domain structures and topologically protected skyrmions [13,14].

Despite intense studies, a deeper understanding of the physics in FGT, attributed to an apparent dichotomy of localized and itinerant electrons, has remained elusive. This has led to debate on whether the magnetic ground state is a simple FM and how to form robust theoretical models. First of all, the Stoner exchange splitting is unlikely to be the sole driving force behind the magnetic ordering; instead, the interaction among localized moments may play an important role [15]. Second, strong electronic correlations are essential to account for magnetic and thermodynamic properties [16]. Akin to iron-based superconductors [17–19], the intra-atomic Hund coupling may be more relevant in this respect than close proximity to a Mott-critical regime [20]. Furthermore, heavy-fermion behavior has been assigned to FGT based on experimental signatures below a characteristic temperature [21], such as large mass renormalization [22] and Kondo screening [23]. Understanding magnetism in FGT and its conjunction with unique electronic properties renders an extensive investigation of energy- and momentum-resolved magnetic responses necessary.

In this Letter, we show that in FGT antiferromagnetic (AFM) spin fluctuations coexist with FM and explicate the behavior through an orbital selective Mott transtion (OSMT) that stabilizes both itinerant and local magnetism. This behavior is revealed experimentally through the static and dynamic magnetic response in neutron scattering measurements that shows continuous rod-like magnetic excitations emerging with characteristic wave vectors centered around the K point. We explain the underlying mechanisms with realistic dynamical mean-field theory (DMFT) calculations that reveal a rare OSMT occurs and drives the AFM behavior [24,25]. Our methodology leads to pinpointing the twofold-degenerate Fe-e'_g orbitals of the Fe($3d$) shell as key behind both the magnetic transition and the OSMT. The multi-orbital character in FGT can explain the observations of local and itinerant physics and competing magnetism, as well as provide insights into potential Kondo behavior.

FGT crystallizes in the hexagonal space group $P6_3/mmc$ [22,26–28], containing two inequivalent Fe crystallographic sites, Fe^{I} and Fe^{II} in Figs. 1(a) and 1(b). Depending on synthesis conditions, the vacancy concentration on the Fe^{II} site can vary up to 30% without changing the average crystal symmetry [28], while no apparent vacancy is found on the Fe^{I} sites. A near-stoichiometric sample of FGT enters a

*baix@ornl.gov
†frank.lechermann@ruhr-uni-bochum.de
‡caldersa@ornl.gov

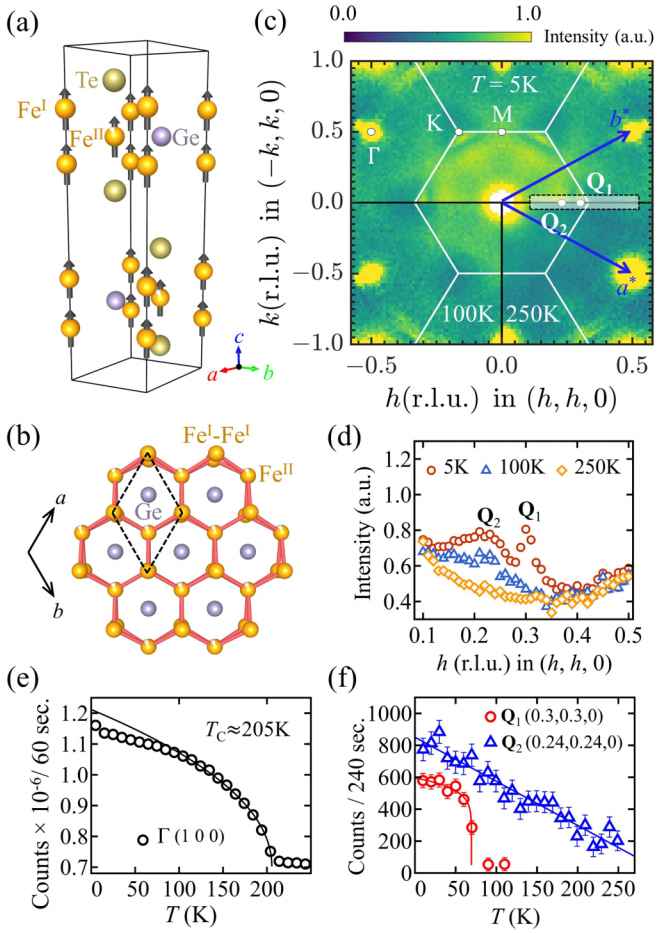

FIG. 1. Elastic neutron scattering data showing FM and AFM static magnetic correlations in $Fe_{2.85}GeTe_2$. (a) Crystal structure and FM spin state of $Fe^{I}_2Fe^{II}_{1-x}GeTe_2$. (b) Single layer view, where the Fe atoms form a decorated honeycomb lattice. The dashed lines indicate the unit cell. (c) Low-Q elastic scattering with $l = 0.0 \pm 0.05$ r.l.u. The white lines are Brillouin zone boundaries. The shaded region indicates the line cuts along the [110] direction integrated over $k = 0.0 \pm 0.02$ r.l.u., shown in the panel (d). Intensity at the (e) FM zone center Γ and (f) the AFM positions $\mathbf{Q}_1$ and $\mathbf{Q}_2$ as a function of temperature. Black and red curves are power-law fits of the data. A linear background are fitted and removed for order-parameter data at $\mathbf{Q}_1$ [Fig. S5]. The paramagnetic background at 250 K is removed at $\mathbf{Q}_2$ and the data offset by 200 for clarity.

FM phase with a strong c-axis anisotropy below the Curie temperature $T_C \approx 230$ K, which is suppressed with increasing vacancy concentration [28]. The critical temperature can also be tuned by chemical doping [29,30] and hydrostatic pressure [31,32]. Single crystals of FGT used in this study were synthesized using a self-flux method with a starting composition of Fe_6GeTe_9 and a maximum temperature of 1160 °C [28,29]. A large single crystal of ∼1g with flat c-surfaces was selected [Fig. S3] and aligned in the (hk0) scattering plane for all neutron experiments. A power-law fit to the temperature evolution of FM Bragg intensity yields a Curie temperature of $T_C = 205(1)$ K [Fig. 1(e)], consistent with a vacancy concentration of $x \sim 0.15$ [28]. This $Fe_{2.85}GeTe_2$ composition therefore has significantly less vacancies than previous inelastic neutron studies [33]. See Supplementary Secs. S1 and S2 [34] for further thermodynamic characterizations and experimental details (see also, Refs. [35–40] therein).

The elastic magnetic response is mapped out in Fig. 1(c) that uncovers AFM correlations developing at low temperatures within the previously observed FM phase. An orthogonal coordinate frame $\{h\mathbf{a}^* + h\mathbf{b}^*, -k\mathbf{a}^* + k\mathbf{b}^*, l\mathbf{c}^*\}$ is used to present data in momentum space, with a generic momentum transfer labeled by $\mathbf{Q} = (h - k, h + k, l)$. At $T = 5$ K, two AFM features near the K point at $\mathbf{Q}_1 = (0.3, 0.3, 0)$ and $\mathbf{Q}_2 = (0.24, 0.24, 0)$ are observed [Figs. 1(c)–1(d)]. Scattering at $\mathbf{Q}_1$ appears to be a weak Bragg reflection with an Ising-type order-parameter temperature dependence (critical exponent ∼ 0.125), which disappears above $T_N = 70(1)$ K [Fig. 1(f)]. $\mathbf{Q}_1$ has an anisotropic peak shape with a narrow width in the [110] direction. The second feature is broad diffuse scattering near $\mathbf{Q}_2$ that persists to higher temperatures [Fig. 1(d)]. The intensity distribution remains mostly unchanged at $l = 0$ and 0.5 r.l.u. [Fig. S4], reflecting a dominant 2D character. Tracking the temperature dependence of scattering intensity at $\mathbf{Q}_2$ shows a linear decrease with increasing temperature up to room temperature.

To investigate the dynamical signature of the observed magnetic correlations, we leverage inelastic neutron scattering on the large single crystal. The results are summarized in Fig. 2. As observed on measurements from samples with more Fe vacancies [33], there are in-plane spin waves consistent with FM ordering. These are well-resolved in momentum space below ∼8 meV but significantly dampen as they enter the Stoner-like continuum at high energies. The magnetic signals may extend to above 100 meV energy transfer [Fig. S8]. No significant difference is observed for the low-energy FM spin waves in the ordered phase between 5 and 155 K after the Bose factor $(1 - \exp(-E/k_BT))^{-1}$ is removed [Fig. 2(c)]. As expected, they become more damped in the paramagnetic phase at $T = 250$ K. Systematic temperature evolution of the FM excitations are also observed in the out-of-plane directions [Fig. S11]. Our linear spin-wave modeling suggests a rather small exchange coupling between Fe^{I} and Fe^{II} sites, and differ from earlier neutron-scattering studies [33,47] and DFT calculations [3,48].

Of most significance, the inelastic neutron data reveals an AFM dynamical response in FGT, in accordance with the measured AFM elastic signals. Continuous rod-like excitations emerge near the K point of the hexagonal Brillouin zone at $T = 5$ K [Fig. 2(a)]. Strikingly, they are removed at $T = 155$ K well below the Curie temperature $T_C = 205(1)$ K, in sharp contrast with the FM spin waves, indicating previously unseen competing AFM interactions. See Figs. S6 and S7 for more details on the temperature dependence. A close inspection of the low-Q region in a constant energy cut at $E = 4 \pm 1$ meV, [Fig. 2(b)], reveals that the inelastic signals extend from the K point to the Γ point, covering both AFM $\mathbf{Q}_1$ and $\mathbf{Q}_2$ positions observed in the elastic channel. Data collected with a lower incident neutron energy $E_i = 25$ meV shows that the signal is gapless within the instrumental resolution of 0.65 meV [Fig. S8]. Applying a magnetic field of $\mu_0 H = 4$ T along the c axis did not yield clear changes in either FM and AFM magnetic excitations [Fig. S9], therefore it is likely that the dominant effect of the field is to align the

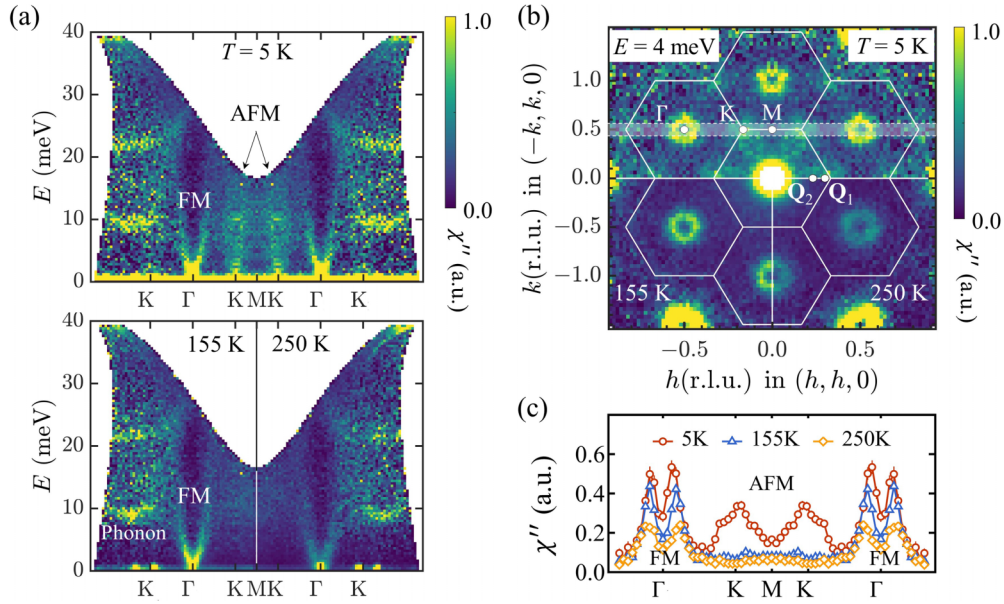

FIG. 2. Inelastic neutron-scattering data of $Fe_{2.85}GeTe_2$ showing coexistence of FM and AFM excitations. The Bose factor is divided out in all panels, giving the imaginary part of the dynamical susceptibility χ''. (a) Temperature dependence of energy- and momentum-resolved excitations at $k = 0.5 \pm 0.05$ r.l.u. and $l = 0.0 \pm 0.3$ r.l.u.. The optical modes around 10 and 20 meV are attributed to phonons, see Sec. S6 for comparison with DFT-calculated phonon spectra and Refs. [41–46] therein for technical details. (b) Low-Q constant-energy cut at $E = 4 \pm 1$ meV. The white lines are Brillouin zone boundaries. (c) Line cuts along the [110] direction at $k = 0.5 \pm 0.1$ r.l.u. and $E = 4 \pm 1$ meV.

ferromagnetic domains without changing microscopic magnetic correlations.

To provide insight into the mechanisms driving the coexisting magnetism observed experimentally we performed charge self-consistent DFT+DMFT [49–51] calculations (see also Refs. [52–60] in Supplementary Information [34]), and the results are summarized in Fig. 3. Finite doping is realized by the virtual-crystal approximation (VCA) originating from the Fe^{II} site. The Fe($3d$) orbitals define the correlated subspace, with Hubbard $U = 5$ eV and Hund-rule coupling $J_H = 0.7$ eV, in line with previous calculations [16]. Due to the hexagonal symmetry, the respective Fe five-fold states split into three classes; a d_{z^2}-like a_{1g} orbital, as well as two degenerate e'_g and two degenerate e_g orbitals (for more details see Sec. S4).

Below the FM transition, $T = 195$ K in Fig. 3(a), the electronic spectral weight at low energy is reduced and shifted to sidebands at $\sim \pm 0.2$ eV. Right at the Fermi level ε_F a pseudogap(-like) regime becomes visible. For $T = 100$ K this regime becomes more pronounced and an OSMT in the $\{e_g, e'_g\}$ orbital sector has occured, while the a_{1g} sector remains metallic. Sharp low-energy $\{e_g, e'_g\}$ resonances are reappearing at even lower T, here shown at $T = 50$ K, suggesting a Kondo coupling between the $\{e_g, e'_g\}$ localized states and the itinerant a_{1g} orbitals. The OSMT physics is most strongly realized on the Fe^{I} sites and becomes weaker for the larger doping $\delta = 0.25$.

The OSMT-driven physics leads to a specific correlation-induced contribution to the local-moment formation in FGT. And this contribution gives rise to emerging AFM fluctations known for Mott-critical systems. The **q**-dependent spin susceptibility $\chi_s^{(0)}$ in Fig. 3(b) shows the growth of these AFM fluctuations (rising intensity at the zone boundary) with lowering T, as also observed experimentally (cf. Fig. 2). Further in agreement with the experimental data, the amplitude is somewhat larger around the K point than at the M point (see Sec. S4). The **k**-resolved features of the correlated electronic structure at low energy are visualized in Fig. 3(c) for ambient T with a fatspec representation, i.e., spectral weight colored according to the respective Fe($3d$) orbital weight. Close to Γ the e'_g orbitals show flattened dispersion, which may be part of the root for the FM instability. A Dirac(-like) crossing point with substantial a_{1g} weight is located at K because of the hexagonal in-plane lattice structure.

The multisheet interacting Fermi surface (FS) displays a rather intricate topology. This complexity is reduced in the low-T phase at 50 K [see Fig. 3(d)], where two dominant FS sheets around Γ are established. Note that the outer sheet actually represents two entangled sub-sheets. Subtle states are encountered right at Γ and at K, but a sharp single-level feature near Γ may connect to Kondo physics. Flat dispersions further above and below the Fermi level can also be observed along M-K. The interacting FS and the additionally revealed **k**-dependent features at low energy are in good agreement with angle-resolved photoemission data [21]. The Fe ordered moments (see Sec. S4) become smaller by ~20% for $\delta = 0.25$, in line with the experimental trend [28]. This reduction with higher hole doping may be attributed to the parallel decrease of the OSMT strength.

Concerning the origin of the OSMT in FGT, differences in the respective orbital-resolved Fe($3d$) fillings and dispersions seem most crucial. The Fe^{I}-a_{1g} orbital shows a pronounced bonding-antibonding splitting and is most itinerant with electron filling $n_{a_{1g}} \sim 1.5$, whereas the e'_g orbitals become integer filled with $n_{e'_g} \sim 3$ in the interacting regime. The filling of the e_g orbitals is nominally somewhat below three electrons, but their more ligand-hybridized character renders an obvious

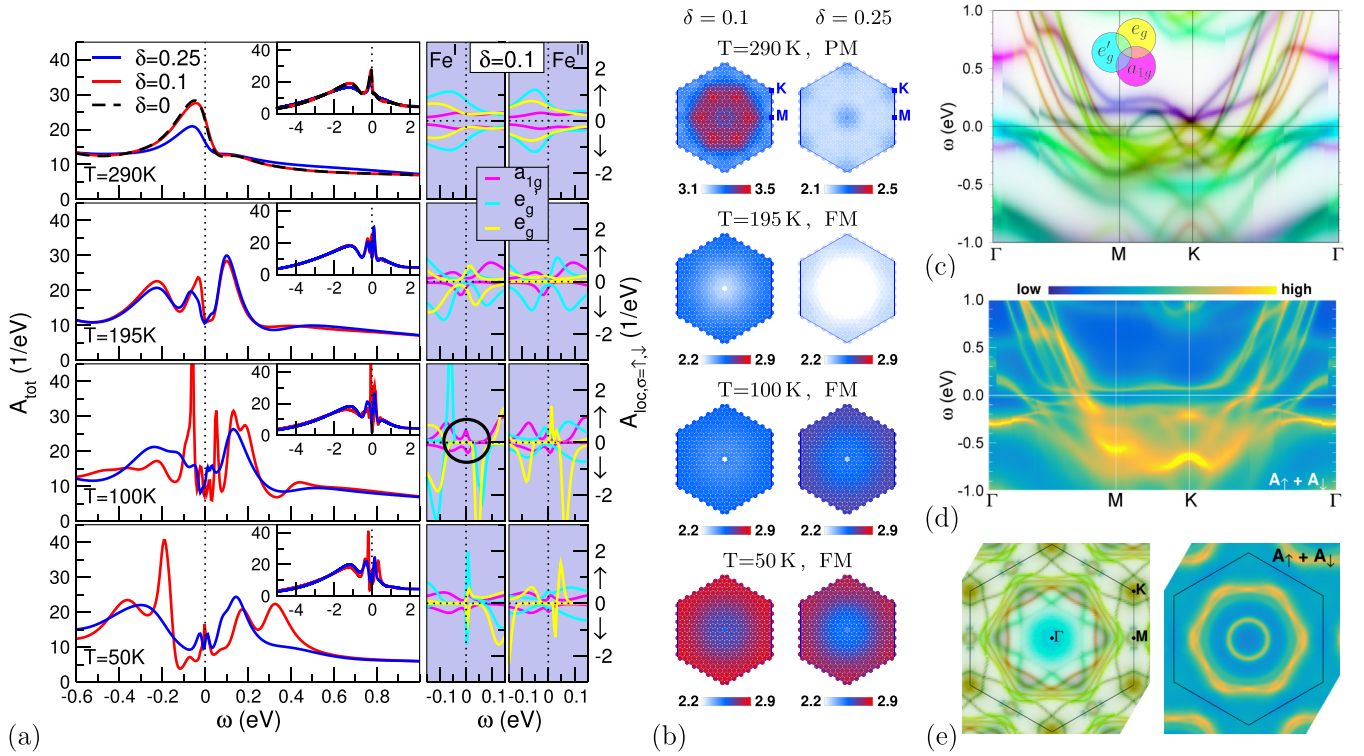

FIG. 3. DFT+DMFT results for $Fe_{3-\delta}GeTe_2$, where $\delta = x$ is the VCA doping level. (a) Total (left) and local Fe($3d$) (spin-)orbital-resolved (right) spectral function $A(\omega)$ for different δ and T. Left insets: larger energy window. Black circle for $T = 100$ K highlights the OSMT scenario. (b) T-dependent Lindhard spin susceptibility $\chi_s^{(0)}(\mathbf{q}, \omega = 0)$ for $\delta = 0.1$,0.25. (c, d) $\mathbf{k}$-resolved spectral-function properties for $\delta = 0.1$. (c) $A(\mathbf{k}, \omega)$ along high-symmetry lines in a Fe($3d$) fatspec representation at $T = 290$ K. Mixed orbital weight appears as the accordingly mixed colors (see color scheme in graph). (d) Spin-summed $A(\mathbf{k}, \omega)$ for $T = 50$ K. (e) $k_z = 0$ FS for $T = 290$ K in fatspec representation (left) and spin-summed intensity for $T = 50$ K (right).

site distinction difficult. The OSMT is thus driven from the e'_g sector and e_g seemingly locks in. Hence, interestingly, the e'_g orbitals are apparently the key behind both the FM transition *and* OSMT. On the more ligand-affected Fe^{II} site, the strong orbital differentiation is smeared out, also due to the direct onsite vacancies. Note that the present five-orbital OSMT scenario with three electrons in the twofold-degenerate e'_g orbitals has to involve the Hund J_H in a more subtle manner than in conventional OSMT candidates, such as ruthenates [25]. This may also be inferred from the small $\sim 100 - 200$ meV charge gap obtained here for the localized $\{e'_g, e_g\}$ states.

Considering the experimental and theoretical results presented here on FGT allows new insights into its exotic and diverse behavior. The OSMT naturally explains the coexistence of localized and itinerant electrons in strongly correlated FGT by providing a multi-orbital character to separately host these behaviors. Moreover, initially a general connection between OSMT and heavy-fermion physics was made in Ref. [61]. While the connection may be subtle [62–64], an example is found in the direct fitting for the f-electron material UPt_3 [65]. The orbital-selective scenario revealed here for FGT provides a natural origin for the measured heavy-fermion signatures [21–23]. Kinetic exchange within this Mott-critical subspace then drives nearest-neighbor AFM fluctuations, which manifests in the spin-susceptibility enhancement at the BZ boundary observed experimentally and theoretically here and debated in the literature. Looking forward, as the low-temperature DFT+DMFT treatment of the realistic system is hindered by computational limitations, further details and cutting-edge data on the OSMT-based interplay between Kondo screening and magnetic order/fluctuations have to be addressed in tailored model Hamiltonian studies.

In conclusion, an orbital-selective Mott transition has been shown to drive the emergent properties in FGT. This provides a singular multi-orbital character to this material, which both reconciles the apparent dual nature of local and itinerant magnetism and explains the observation of AFM fluctuations from the presented neutron-scattering data. Unexpected signatures of heavy fermion physics in previous studies of FGT have proven to be challenging to rationalize, however the uncovering of OSMT physics provides a clear route for the solution of this problem. The results presented here represent a significant advancement in understanding the coexistence of itinerant and local moments in a canonical quasi-2D vdW ferromagnetic material and may have relevant consequences for spin and orbital dependent electronic functions within wider spintronic and topological transport research.

X.B. thanks Cristian Batista for valuable discussions. Sample synthesis and characterization (A.F.M.) was supported by the U.S. Department of Energy, Office of Science, Basic Energy Sciences, Materials Sciences and Engineering Division. This research used resources at the High Flux Isotope Reactor

and Spallation Neutron Source, a DOE Office of Science User Facility operated by the Oak Ridge National Laboratory. F.L. acknowledges support from the European XFEL and the Center for Computational Quantum Physics of the Flatiron Institute under the Simons Award ID 825141. Computations were performed at the JUWELS Cluster of the Jülich Supercomputing Centre (JSC) under Projects No. hhh08 and No. miqs.

[1] K. S. Burch, D. Mandrus, and J.-G. Park, Nature (London) **563**, 47 (2018).
[2] H. Li, S. Ruan, and Y.-J. Zeng, Adv. Mater. **31**, 1900065 (2019).
[3] Y. Deng, Y. Yu, Y. Song, J. Zhang, N. Z. Wang, Z. Sun, Y. Yi, Y. Z. Wu, S. Wu, J. Zhu *et al.*, Nature (London) **563**, 94 (2018).
[4] S. Liu, X. Yuan, Y. Zou, Y. Sheng, C. Huang, E. Zhang, J. Ling, Y. Liu, W. Wang, C. Zhang *et al.*, npj 2D Mater. Appl. **1**, 30 (2017).
[5] Z. Fei, B. Huang, P. Malinowski, W. Wang, T. Song, J. Sanchez, W. Yao, D. Xiao, X. Zhu, A. F. May *et al.*, Nat. Mater. **17**, 778 (2018).
[6] R. Roemer, C. Liu, and K. Zou, npj 2D Mater. Appl. **4**, 33 (2020).
[7] X. Wang, J. Tang, X. Xia, C. He, J. Zhang, Y. Liu, C. Wan, C. Fang, C. Guo, W. Yang *et al.*, Sci. Adv. **5**, eaaw8904 (2019).
[8] J. Xu, W. A. Phelan, and C.-L. Chien, Nano Lett. **19**, 8250 (2019).
[9] G. Zheng, W.-Q. Xie, S. Albarakati, M. Algarni, C. Tan, Y. Wang, J. Peng, J. Partridge, L. Farrar, J. Yi *et al.*, Phys. Rev. Lett. **125**, 047202 (2020).
[10] Y. Wang, C. Xian, J. Wang, B. Liu, L. Ling, L. Zhang, L. Cao, Z. Qu, and Y. Xiong, Phys. Rev. B **96**, 134428 (2017).
[11] K. Kim, J. Seo, E. Lee, K.-T. Ko, B. Kim, B. G. Jang, J. M. Ok, J. Lee, Y. J. Jo, W. Kang *et al.*, Nat. Mater. **17**, 794 (2018).
[12] Y. Liu, E. Stavitski, K. Attenkofer, and C. Petrovic, Phys. Rev. B **97**, 165415 (2018).
[13] Y. Wu, S. Zhang, J. Zhang, W. Wang, Y. L. Zhu, J. Hu, G. Yin, K. Wong, C. Fang, C. Wan *et al.*, Nat. Commun. **11**, 3860 (2020).
[14] B. Ding, Z. Li, G. Xu, H. Li, Z. Hou, E. Liu, X. Xi, F. Xu, Y. Yao, and W. Wang, Nano Lett. **20**, 868 (2020).
[15] X. Xu, Y. W. Li, S. R. Duan, S. L. Zhang, Y. J. Chen, L. Kang, A. J. Liang, C. Chen, W. Xia, Y. Xu, P. Malinowski, X. D. Xu, J. H. Chu, G. Li, Y. F. Guo, Z. K. Liu, L. X. Yang, and Y. L. Chen, Phys. Rev. B **101**, 201104(R) (2020).
[16] J.-X. Zhu, M. Janoschek, D. S. Chaves, J. C. Cezar, T. Durakiewicz, F. Ronning, Y. Sassa, M. Mansson, B. L. Scott, N. Wakeham, E. D. Bauer, and J. D. Thompson, Phys. Rev. B **93**, 144404 (2016).
[17] A. Tamai, A.Y. Ganin, E. Rozbicki, J. Bacsa, W. Meevasana, P. D. C. King, M. Caffio, R. Schaub, S. Margadonna, K. Prassides, M. J. Rosseinsky, and F. Baumberger, Phys. Rev. Lett. **104**, 097002 (2010).
[18] I. Mazin, D. J. Singh, M. D. Johannes, and M.-H. Du, Phys. Rev. Lett. **101**, 057003 (2008).
[19] A. Georges, L. de' Medici, and J. Mravlje, Annu. Rev. Condens. Matter Phys. **4**, 137 (2013).
[20] M. Corasaniti, R. Yang, K. Sen, K. Willa, M. Merz, A. A. Haghighirad, M. Le Tacon, and L. Degiorgi, Phys. Rev. B **102**, 161109(R) (2020).
[21] Y. Zhang, H. Lu, X. Zhu, S. Tan, W. Feng, Q. Liu, W. Zhang, Q. Chen, Y. Liu, X. Luo *et al.*, Sci. Adv. **4**, eaao6791 (2018).
[22] B. Chen, J. Yang, H. Wang, M. Imai, H. Ohta, C. Michioka, K. Yoshimura, and M. Fang, J. Phys. Soc. Jpn. **82**, 124711 (2013).
[23] M. Zhao, B.-B. Chen, Y. Xi, Y. Zhao, H. Xu, H. Zhang, N. Cheng, H. Feng, J. Zhuang, F. Pan *et al.*, Nano Lett. **21**, 6117 (2021).
[24] J. Goodenough and S. Ramasesha, Mater. Res. Bull. **17**, 383 (1982).
[25] V. I. Anisimov, I. A. Nekrasov, D. E. Kondakov, T. M. Rice, and M. Sigrist, Eur. Phys. J. B **25**, 191 (2002).
[26] H.-J. Deiseroth, K. Aleksandrov, C. Reiner, L. Kienle, and R. K. Kremer, Eur. J. Inorg. Chem. **2006**, 1561 (2006).
[27] V. Y. Verchenko, A. A. Tsirlin, A. V. Sobolev, I. A. Presniakov, and A. V. Shevelkov, Inorg. Chem. **54**, 8598 (2015).
[28] A. F. May, S. Calder, C. Cantoni, H. Cao, and M. A. McGuire, Phys. Rev. B **93**, 014411 (2016).
[29] G. Drachuck, Z. Salman, M. W. Masters, V. Taufour, T. N. Lamichhane, Q. Lin, W. E. Straszheim, S. L. Bud'Ko, and P. C. Canfield, Phys. Rev. B **98**, 144434 (2018).
[30] C.-K. Tian, C. Wang, W. Ji, J.-C. Wang, T.-L. Xia, L. Wang, J.-J. Liu, H.-X. Zhang, and P. Cheng, Phys. Rev. B **99**, 184428 (2019).
[31] X. Wang, Z. Li, M. Zhang, T. Hou, J. Zhao, L. Li, A. Rahman, Z. Xu, J. Gong, Z. Chi *et al.*, Phys. Rev. B **100**, 014407 (2019).
[32] S. Ding, Z. Liang, J. Yang, C. Yun, P. Zhang, Z. Li, M. Xue, Z. Liu, G. Tian, F. Liu *et al.*, Phys. Rev. B **103**, 094429 (2021).
[33] S. Calder, A. I. Kolesnikov, and A. F. May, Phys. Rev. B **99**, 094423 (2019).
[34] See Supplemental Material at http://link.aps.org/supplemental/10.1103/PhysRevB.106.L180409 for more experimental data and theoretical analysis.
[35] F. Ye, Y. Liu, R. Whitfield, R. Osborn, and S. Rosenkranz, J. Appl. Crystallogr. **51**, 315 (2018).
[36] G. Granroth, A. Kolesnikov, T. Sherline, J. Clancy, K. Ross, J. Ruff, B. Gaulin, and S. Nagler, J. Phys.: Conf. Ser. **251**, 012058 (2010).
[37] D. L. Abernathy, M. B. Stone, M. Loguillo, M. Lucas, O. Delaire, X. Tang, J. Lin, and B. Fultz, Rev. Sci. Instrum. **83**, 015114 (2012).
[38] O. Arnold, J.-C. Bilheux, J. Borreguero, A. Buts, S. I. Campbell, L. Chapon, M. Doucet, N. Draper, R. F. Leal, M. Gigg *et al.*, Nucl. Instrum. Methods Phys. Res., Sect. A **764**, 156 (2014).
[39] R. Ewings, A. Buts, M. Le, J. Van Duijn, I. Bustinduy, and T. Perring, Nucl. Instrum. Methods Phys. Res., Sect. A **834**, 132 (2016).
[40] S. Toth and B. Lake, J. Phys.: Condens. Matter **27**, 166002 (2015).
[41] G. Kresse and J. Furthmüller, Phys. Rev. B **54**, 11169 (1996).
[42] P. E. Blöchl, Phys. Rev. B **50**, 17953 (1994).
[43] G. Kresse and D. Joubert, Phys. Rev. B **59**, 1758 (1999).
[44] J. P. Perdew and A. Zunger, Phys. Rev. B **23**, 5048 (1981).

[45] H. L. Zhuang, P. R. C. Kent, and R. G. Hennig, Phys. Rev. B **93**, 134407 (2016).
[46] Y. Cheng, L. Daemen, A. Kolesnikov, and A. Ramirez-Cuesta, J. Chem. Theory Comput. **15**, 1974 (2019).
[47] C. Trainer, O. R. Armitage, H. Lane, L. C. Rhodes, E. Chan, I. Benedičič, J. A. Rodriguez-Rivera, O. Fabelo, C. Stock, and P. Wahl, Phys. Rev. B **106**, L081405 (2022).
[48] S. W. Jang, H. Yoon, M. Y. Jeong, S. Ryee, H.-S. Kim, and M. J. Han, Nanoscale **12**, 13501 (2020).
[49] S. Y. Savrasov, G. Kotliar, and E. Abrahams, Nature (London) **410**, 793 (2001).
[50] L. V. Pourovskii, B. Amadon, S. Biermann, and A. Georges, Phys. Rev. B **76**, 235101 (2007).
[51] D. Grieger, C. Piefke, O. E. Peil, and F. Lechermann, Phys. Rev. B **86**, 155121 (2012).
[52] C. Elsässer, N. Takeuchi, K. M. Ho, C. T. Chan, P. Braun, and M. Fähnle, J. Phys.: Condens. Matter **2**, 4371 (1990).
[53] F. Lechermann, F. Welsch, C. Elsässer, C. Ederer, M. Fähnle, J. M. Sanchez, and B. Meyer, Phys. Rev. B **65**, 132104 (2002).
[54] B. Amadon, F. Lechermann, A. Georges, F. Jollet, T. O. Wehling, and A. I. Lichtenstein, Phys. Rev. B **77**, 205112 (2008).
[55] V. I. Anisimov, I. V. Solovyev, M. A. Korotin, M. T. Czyżyk, and G. A. Sawatzky, Phys. Rev. B **48**, 16929 (1993).
[56] P. Werner, A. Comanac, L. de' Medici, M. Troyer, and A. J. Millis, Phys. Rev. Lett. **97**, 076405 (2006).
[57] O. Parcollet, M. Ferrero, T. Ayral, H. Hafermann, I. Krivenko, L. Messio, and P. Seth, Comput. Phys. Commun. **196**, 398 (2015).
[58] P. Seth, I. Krivenko, M. Ferrero, and O. Parcollet, Comput. Phys. Commun. **200**, 274 (2016).
[59] M. Jarrell and J. E. Gubernatis, Phys. Rep. **269**, 133 (1996).
[60] H. J. Vidberg and J. W. Serene, J. Low Temp. Phys. **29**, 179 (1977).
[61] L. de' Medici, A. Georges, G. Kotliar, and S. Biermann, Phys. Rev. Lett. **95**, 066402 (2005).
[62] C. Pépin, Phys. Rev. Lett. **98**, 206401 (2007).
[63] L. De Leo, M. Civelli, and G. Kotliar, Phys. Rev. Lett. **101**, 256404 (2008).
[64] M. Vojta, J. Low Temp. Phys. **161**, 203 (2010).
[65] G. Zwicknagl, A. N. Yaresko, and P. Fulde, Phys. Rev. B **65**, 081103(R) (2002).